BIOCHEMISTRY
including biophysical chemistry & molecular biology
Article

Biochemistry **2011,** *50,* 1535–1544 1535
DOI: 10.1021/bi101170p

Nickel(II) Chelatase Variants Directly Evolved from Murine Ferrochelatase: Porphyrin Distortion and Kinetic Mechanism†

Neil R. McIntyre,‡ Ricardo Franco,§ John A. Shelnutt,*,∥,⊥ and Gloria C. Ferreira*,‡,#,△

‡*Department of Molecular Medicine, College of Medicine,* #*H. Lee Moffitt Cancer Center and Research Institute, and* △*Department of Chemistry, University of South Florida, Tampa, Florida, 33612, United States,* §*REQUIMTE, Departamento de Química, Faculdade de Ciências e Tecnologia, Universidade Nova de Lisboa, 2829-516 Caparica, Portugal,* ∥*Advanced Materials Laboratory, Sandia National Laboratories, Albuquerque, New Mexico 87185-1349, United States, and* ⊥*Department of Chemistry, University of Georgia, Athens, Georgia 30602-2556, United States*

Received July 22, 2010; Revised Manuscript Received December 30, 2010

ABSTRACT: The heme biosynthetic pathway culminates with the ferrochelatase-catalyzed ferrous iron chelation into protoporphyrin IX to form protoheme. The catalytic mechanism of ferrochelatase has been proposed to involve the stabilization of a nonplanar porphyrin to present the pyrrole nitrogens to the metal ion substrate. Previously, we hypothesized that the ferrochelatase-induced nonplanar distortions of the porphyrin substrate impose selectivity for the divalent metal ion incorporated into the porphyrin ring and facilitate the release of the metalated porphyrin through its reduced affinity for the enzyme. Using resonance Raman spectroscopy, the structural properties of porphyrins bound to the active site of directly evolved Ni^{2+}-chelatase variants are now examined with regard to the mode and extent of porphyrin deformation and related to the catalytic properties of the enzymes. The Ni^{2+}-chelatase variants (S143T, F323L, and S143T/F323L), which were directly evolved to exhibit an enhanced Ni^{2+}-chelatase activity over that of the parent wild-type ferrochelatase, induced a weaker saddling deformation of the porphyrin substrate. Steady-state kinetic parameters of the evolved variants for Ni^{2+}- and Fe^{2+}-chelatase activities increased compared to those of wild-type ferrochelatase. In particular, the reduced porphyrin saddling deformation correlated with increased catalytic efficiency toward the metal ion substrate (Ni^{2+} or Fe^{2+}). The results lead us to propose that the decrease in the induced protoporphyrin IX saddling mode is associated with a less stringent metal ion preference by ferrochelatase and a slower porphyrin chelation step.

Heme is a critical cofactor for many biological processes, as its physiological roles span a unique catalogue of chemical functions from oxygen transport (*1*, *2*), binding and sensing of diatomic molecules (*3*), electron transfer (*2*), extracellular signaling (*4*), regulation of transcription and translation (*5*), miRNA processing (*6*), and xenobiotic detoxification (*7*) to catalysis (*1*). The heme biosynthetic pathway terminates with the chelation of a ferrous iron by protoporphyrin IX in a reaction catalyzed by ferrochelatase (E.C. 4.99.1.1, protoheme lyase) (*8*−*10*). Decreased ferrochelatase activity is an hallmark of the blood disorder erythropoeitic protoporphyria (*11*), and downregulation of transcription of the human ferrochelatase gene and consequent diminished ferrochelatase activity and protoporphyrin IX accumulation have been reported to be associated with several types of cancer (e.g., gastric, colon, and rectal) (*12*). The crystal structures of *Bacillus subtilis* (*13*−*16*), human (*17*−*20*), and *Saccharomyces cerevisiae* (*21*) ferrochelatase have been solved; while the oligomeric state for *B. subtilis* ferrochelatase (monomer) differs from that of the human and yeast enzymes (homodimer), the monomeric topology displays high structural similarity across taxa. In all currently solved structures, the monomeric unit contains two domains, each with a Rossman-type fold covering four parallel β-sheets flanked by α-helices (*13*, *20*, *21*). A cleft defined by structural elements from the two domains accommodates the porphyrin-binding and putative metal-binding sites (*13*, *21*).

Although the physiologically relevant reaction catalyzed by ferrochelatase is the chelation of ferrous iron (Fe^{2+}) into the porphyrin ring, the enzyme can chelate other divalent metals (e.g., Zn^{2+}, Co^{2+}, and Cu^{2+}) (*8*, *9*, *21*−*23*). The catalytic mechanism of ferrochelatase for ferrous iron insertion into porphyrin is recognized to involve the stabilization of a nonplanar conformation of the porphyrin macrocycle (*8*, *24*). This concept of an adopted nonplanar deformation upon substrate binding to ferrochelatase has been substantiated with a diverse series of theoretical (*25*) and experimental studies (*26*−*29*) including those involving catalytic antibodies raised against *N*-methylmesoporphyrin IX, a proposed transition state analogue of the ferrochelatase-catalyzed reaction (*28*−*30*). The elicited antibody binds, distorts, and stabilizes the nonalkylated porphyrin substrate toward a similar geometry to that of the *N*-methylmesoporphyrin IX hapten, thereby increasing the rates of divalent metal chelation into porphyrin (*29*). Further, with the X-ray crystal structure of the Michaelis complex formed between

†This work was supported by National Institutes of Health Grant GM080270 and AHA Grant 0655091B to G.C.F. Sandia is a multiprogram laboratory operated by Sandia Corp., a Lockheed Martin Co., for the United States Department of Energy's National Nuclear Security Administration under Contract DE-AC0494AL85000. FLAD (Luso-American Foundation, Portugal) is gratefully acknowledged for financial support to this work.

*To whom correspondence should be addressed. G.C.F.: telephone, 813-974-5797; fax, 813-974-0504; e-mail, gferreir@health.usf.edu. J.A.S.: telephone, 505-272-7160; fax, 505-272-7077; e-mail, jasheln@unm.edu.

Published on Web 01/11/2011

the ferrochelatase catalytic antibody and the porphyrin substrate, Yin et al. demonstrated that the porphyrin substrate was distorted toward a transition state geometry for metalation (*28*). This finding is in perfect agreement with the "strain theory" proposed by Haldane and Pauling, who postulated that, upon binding to the enzyme, the substrate is strained or distorted (*27*, *31*), the transition state is stabilized, and consequently the activation energy of the reaction is decreased. Accordingly, the catalytic antibody-induced ~30° tilt in pyrrole A of the porphyrin substrate lowered the activation energy barrier for metal ion chelation through stabilization of the transition state conformation in which the pyrrole nitrogen lone pairs were exposed for metal ion coordination (*29*). Recently, transient kinetic analysis of the ferrochelatase-catalyzed reaction led Hoggins et al. to suggest a two-step kinetic mechanism in which substrate binding occurs in a rapid equilibrium with the enzyme; porphyrin metalation occurs as a second and irreversible step (*32*). Direct analysis of metalloporphyrin formation and comparison between the steady-state and transient kinetic results indicated that the rate associated with the metalation step was 10-fold faster than that for product release (*32*). Thus, Hoggins et al. assigned product release as the rate-determining step in the ferrochelatase-catalyzed reaction (*32*).

Among chelatases, the relationship between porphyrin distortion and metal ion specificity is considered paramount to understanding the *raison d'être* for this enzyme class (*24*). Resonance Raman (RR)[1] spectroscopy and X-ray crystallography have been particularly effective for evaluating the contribution of out-of-plane porphyrin distortions to porphyrin metalation catalyzed by ferrochelatase (*33*, *34*) and ferrochelatase catalytic antibodies (*30*). Indeed, using RR spectroscopy, we demonstrated that murine ferrochelatase induces porphyrin distortion even in the absence of the metal ion substrate (*26*, *33*) and, subsequently, determined that decreased induction of the nonplanar (saddled) porphyrin deformation relates to reduced catalytic efficiency of ferrochelatase toward protoporphyrin, when Fe^{2+} was the metal ion substrate (*34*). Briefly, porphyrin binding to ferrochelatase variants with lower catalytic efficiencies than the wild-type enzyme resulted in a decrease in the intensity of the RR out-of-plane vibrational mode γ_{15}, a B_{2u} symmetry (saddling-like) mode associated with an out-of-plane porphyrin deformation. Deformation along this normal coordinate exposes the protons and the lone pairs of the nitrogen atoms of the porphyrin core to the incoming metal ion (*34*). Similarly, RR spectra for mesoporphyrin IX bound to a collection of ferrochelatase catalytic antibodies raised against *N*-methylmesoporphyrin IX indicated that the γ_{15} mode increased in intensity from the germline precursor antibody to the affinity-matured antibody (*30*).

In the present study, using a combination of RR spectroscopy and steady-state kinetics, we investigate the relationship between the type and extent of the enzyme-induced nonplanar porphyrin deformation and the particular divalent metal ion inserted into the porphyrin macrocycle by ferrochelatase. Variants of ferrochelatase that were directly evolved to possess significantly greater Ni^{2+}-chelatase activity than wild-type ferrochelatase induced a less intense γ_{15} line, indicating a less pronounced saddling of the porphyrin substrate than the wild-type enzyme. The reduced saddling undergone by the porphyrin substrate upon binding to the ferrochelatase variants was accompanied by an increase in catalytic efficiencies and turnover numbers for both Ni^{2+} and Fe^{2+} chelation into protoporphyrin IX. Overall, while the rate of metalated porphyrin (NiPP or heme) production increases in the reactions catalyzed by the directly evolved Ni^{2+}-chelatase variants, the rate of the chelation step is expected to be slower due to a more flattened conformation of the porphyrin substrate than in the wild-type ferrochelatase reaction. We propose that the decrease in nonplanar saddling deformation is associated with a less stringent metal ion preference by ferrochelatase.

MATERIALS AND METHODS

Materials. Protoporphyrin IX and Ni^{2+}-protoporphyrin IX were purchased from Frontier Scientific, while hemin was from Sigma Chemicals. Porphyrins were used without further purification. Tween 80 (polyethylene glycol sorbitan monooleate), trizma base ((hydroxymethyl)aminomethane carbonate), bicinchoninic acid protein concentration determination kit, phenylmethylsulfonamide, and nickel chloride were from Sigma Chemicals. Reagents for SDS−PAGE were from Bio-Rad Laboratories. Superdex-200 gel filtration matrix and Ni-NTA agarose resin were purchased from QIAGEN. All other reagents were obtained from Fisher Scientific. All reagents were of the highest available purity.

Protein Purification. Ni^{2+}-chelatase variants (S143T, F323L, and S143T/F323L) were evolved from wild-type murine ferrochelatase to acquire at least 10-fold greater Ni^{2+}-chelatase activity than wild-type ferrochelatase. Briefly, the directed evolution of the Ni^{2+}-chelatase variants involved three "generations" of error-prone PCR (*35*), using a murine ferrochelatase prokaryotic expression vector (*36*) as DNA template, DNA shuffling (*35*, *37*), and selection through high-throughput screening, which was based on a spectrophotometric assay for detection of NiPP (unpublished results). His-tagged wild-type ferrochelatase and Ni^{2+}-chelatase variants were overproduced in *Escherichia coli* BL21(DE3) cells (*36*) and purified as previously described (*38*) with the exception that the NaCl concentration in the equilibration buffer was raised to 0.5 M. Aliquots of ~200 μL of purified proteins (~150 μM) in equilibration buffer (20 mM Tris-HCl, pH 8.0, 10% glycerol, and 0.5 M NaCl) were kept in liquid N_2 until use. Protein concentration was determined by the bicinchoninic acid assay (*39*) with bovine serum albumin as standard. Protein purity was assessed by sodium dodecyl sulfate−polyacylamide gel electrophoresis.

Porphyrin Solutions. All porphyrin solutions were prepared through the sequential addition of 2 N NH_4OH (100 μL), 10% Tween-80 (100 μL), and H_2O (1.8 mL) to the solid porphyrin yielding typically stocks of 2 mM. Prior to collecting the RR spectra, the porphyrin stock solutions were diluted in equilibration buffer such that base and surfactant concentrations were the same among porphyrin samples.

Resonance Raman Spectroscopy. Samples for RR spectra were prepared by mixing 100 μM protein (wild-type ferrochelatase or directly evolved Ni^{2+}-chelatase variants) and 30 μM porphyrin in equilibration buffer (V_f = 100 μL) and incubating on ice for ~20 min. The final concentration of Tween-80 surfactant was adjusted to 12 μM. Following incubation, the samples were transferred into a stoppered 3 × 3 mm^2 cross-section optical cell (NSG Precision Cells). Each spectrum was recorded at room temperature for 2−10 min using 20 mW of laser

[1]Abbreviations: hemin, iron(III) protoporphyrin IX; NiPP, Ni(II) protoporphyrin IX; H_2PP, free base protoporphyrin IX; Fe^{2+}-PP, Fe^{2+}-protoporphyrin IX; RR, resonance Raman.

power. The RR spectra were collected using the 406.7 nm line (Soret excitation) of an INNOVA 304 Kr^+ laser (Coherent) source and a Raman spectrometer as previously described (*26*). The spectrometer was a 0.75 m monochromator with a 512 × 2048 pixel liquid N_2-cooled CCD detector (Instruments, SA). Position mode was used for CCD detection, with each section covering ~500 cm^{-1} of the Raman spectrum without moving the grating. All RR spectra were exported as even-X ASCII files for plotting with SigmaPlot (SPSS). Spectral analysis was performed with the curve fitting program Peakfit (version 4.11, SYSTAT). Lorentzian decomposition of the RR spectra was performed to identify peak parameters (height, area, center, and width) associated with the structure-sensitive lines. For analysis of the saddling-symmetry (B_{2u}) mode γ_{15}, spectra were truncated to the 580−780 cm^{-1} range.

Enzymatic Activity Assay. Steady-state ferrochelatase activity was determined by monitoring the consumption of protoporphyrin IX substrate using Fe^{2+} as the metal ion substrate in a continuous spectrofluorometric assay performed at 30 °C under anaerobic conditions as described previously (*40*). Similarly, Ni^{2+}-chelatase activity was determined fluorometrically by following the consumption of protoporphyrin IX substrate using Ni^{2+} as the metal ion substrate at 30 °C and under aerobic conditions. The reaction assay contained 0.1 M Tris−acetate, pH 8.0, 0.5 M NaCl, 0.1% (v/v) Tween-80, and ~150 nM enzyme. To determine the steady-state kinetic parameters (K_m^{PPIX}, $K_m^{M^{2+}}$, and k_{cat}), the data were analyzed in matrices of six protoporphyrin IX and Fe^{2+} (or Ni^{2+}) concentrations and fitted to the bisubstrate Michaelis−Menten equation (eq 1):

$$\text{rate} = \frac{V_m[\text{PPIX}][M^{2+}]}{K_i^{\text{PPIX}}K_m^{M^{2+}} + K_m^{\text{PPIX}}[M^{2+}] + K_m^{M^{2+}}[\text{PPIX}] + [\text{PPIX}][M^{2+}]} \quad (1)$$

where K_m^{PPIX} and $K_m^{M^{2+}}$ are the Michaelis constants for protoporphyrin IX and the divalent metal ion (Fe^{2+} or Ni^{2+}), respectively, and K_i^{PPIX} is the limiting value of K_m^{PPIX} when the divalent metal ion concentration approaches zero. It should be stressed that under the described experimental conditions (e.g., 0.1 M Tris−acetate, pH 8.0, 0.5 M NaCl, 0.1% (v/v) Tween-80, and Ni^{2+} concentrations lower than 40 μM) no Ni^{2+} substrate inhibition of ferrochelatase was observed.

RESULTS

Binding of H_2PP to Directly Evolved Ni^{2+}-Chelatase Variants. RR spectroscopy was used to examine the binding of free base protoporphyrin IX (H_2PP) to the active site of evolved Ni^{2+}-chelatase variants and that of wild-type murine ferrochelatase. Figure 1 gives the low- (Figure 1A) and high-frequency (Figure 1B) regions of the RR spectra of H_2PP incubated with the Ni^{2+}-chelatase variants at a 0.3 porphyrin:protein molar ratio (Figure 1, spectra c−e). For comparison, the RR spectra of H_2PP in equilibration buffer (Figure 1, spectrum a) and bound to wild-type ferrochelatase (Figure 1, spectrum b) are provided. Clear differences were observed in the RR spectra of H_2PP bound to the Ni^{2+}-chelatase variants in relation to those of H_2PP in the surfactant micellar environment. While the ν_7 line was broad for unbound H_2PP (Figure 1A, spectrum a), it displayed a pronounced narrowing and upshift from 667.7 to 675.0 cm^{-1} when bound to wild-type ferrochelatase (Figure 1A, spectrum b). The ν_7 line also upshifted from 667.7 to 672.9 cm^{-1} upon binding of

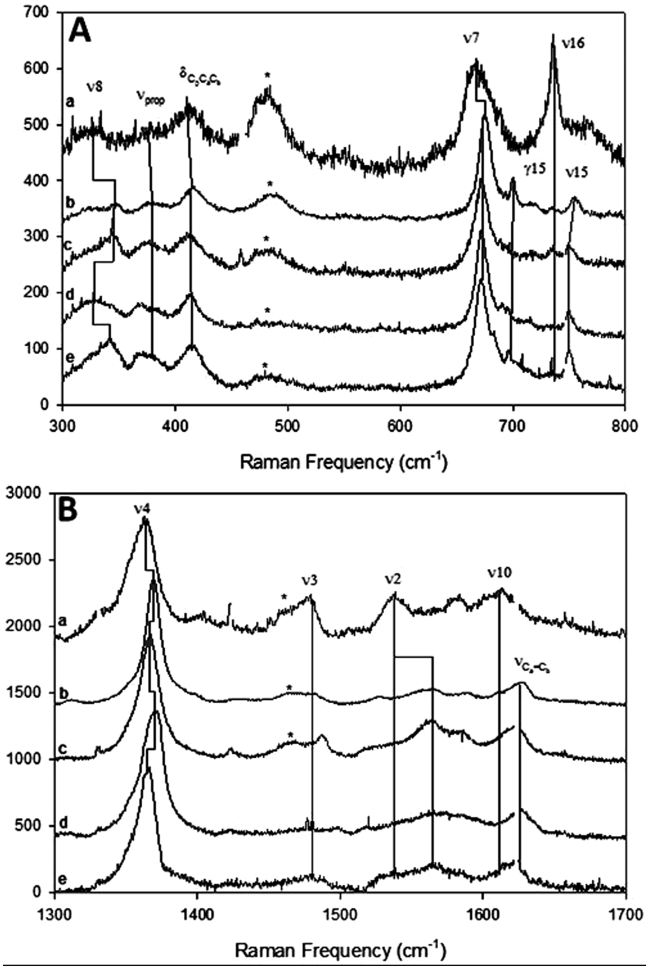

FIGURE 1: Low-frequency (A) and high-frequency (B) regions of the resonance Raman spectra of H_2PP in assay buffer (a), bound to wild-type ferrochelatase (b), and bound to directly evolved Ni^{2+}-chelatase variants (c−g) after incubation with a protein:H_2PP molar ratio of 3. The variants include (c) single mutated variant S143T, (d) single mutated variant F323L, and (e) doubly mutated variant S143T/F323L. Asterisks denote buffer lines. Vibrational modes of the major structure-sensitive lines are labeled.

H_2PP to S143T (Figure 1A, spectrum c) and to 671.9 cm^{-1} upon binding to either F323L (Figure 1A, spectrum d) or S143T/F323L (Figure 1A, spectrum e). H_2PP binding to either wild-type ferrochelatase or the Ni^{2+}-chelatase variants also activated γ_{15} (in the region between 695.5 and 700.3 cm^{-1}) and induced a decrease in the intensity of the ν_{16} line at 735.4 cm^{-1} (Figure 1A, spectrum a vs spectra b−e). The $\delta C_\beta C_a C_b$ bending mode at ~414 cm^{-1}, which was very broad and of low intensity in the spectrum for the unbound H_2PP (Figure 1A, spectrum a), sharpened upon binding of H_2PP to any of the proteins (Figure 1A, spectra b−e). Finally, the upshift and sharpening of ν_8 observed for H_2PP binding to wild-type ferrochelatase (Figure 1A, spectra a and b) were more evident for binding to the S143T and S143T/F323L variants (Figure 1A, spectra c and e).

RR spectra in the high-frequency region (Figure 1B) also displayed significant differences for free H_2PP (Figure 1B, spectrum a) and H_2PP bound to any of the proteins (Figure 1B, spectra b−e). For all proteins, H_2PP binding shifted ν_4 to higher frequencies, although the extent of the shift varied according to the protein. Specifically, the ν_4 line was shifted from 1362.6 cm^{-1} for unbound H_2PP (Figure 1B, spectrum a) to 1370.0 and 1370.9 cm^{-1} for wild-type ferrochelatase- and F323L-bound

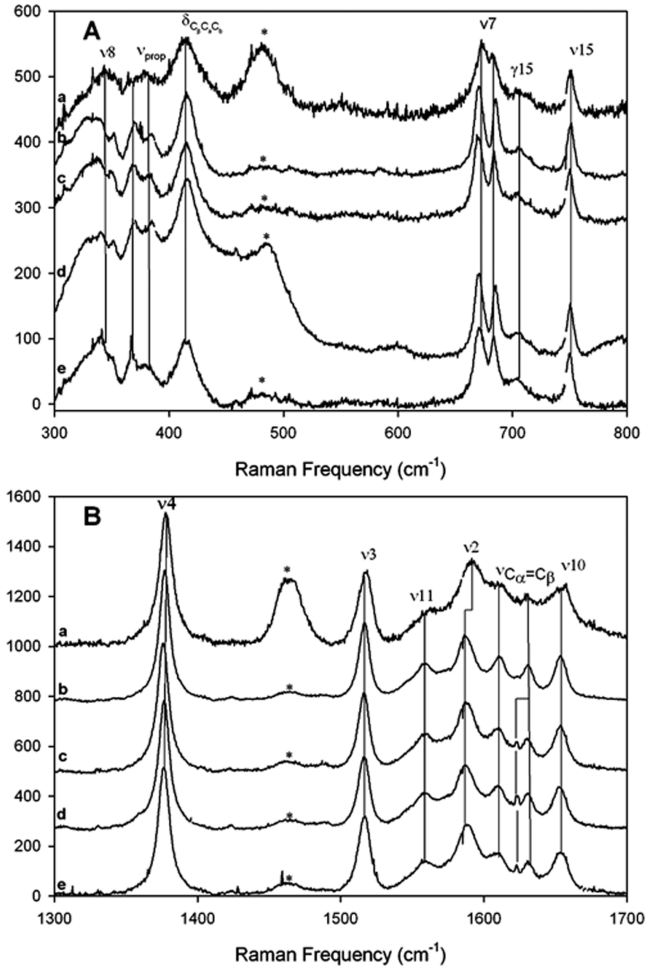

FIGURE 2: Low-frequency (A) and high-frequency (B) regions of the resonance Raman spectra of NiPP in assay buffer (a), bound to wild-type ferrochelatase (b), and bound to directly evolved Ni^{2+}-chelatase variants (c−g) after incubation with a protein:NiPP molar ratio of 3. The variants include (c) singly mutated variant S143T, (d) singly mutated variant F323L, and (e) doubly mutated variant S143T/F323L. Asterisks denote buffer lines and a still unassigned line at 1622 cm^{-1}.

H_2PP, respectively (Figure 1B, spectra b and d); S143T- and S143T/F323L-bound H_2PP gave lower shifts to 1366.7 and 1365.8 cm^{-1}, respectively (Figure 1B, spectra c and e). With the exception of a low-intensity ν_{10} line for H_2PP (*41*, *42*) bound to the S143T/F323L variant (Figure 1B, spectrum e), ν_{10} was very broad and shallow in the other protein spectra (Figure 1B, spectra b−d). The ν_2 line was considerably reduced in intensity and shifted from 1538.3 to 1564.9 cm^{-1} following porphyrin binding to wild-type ferrochelatase and the variants (Figure 1B, spectra b−e). In contrast, intensity of the vinyl stretching mode $\nu_{C\alpha=C\beta}$ of H_2PP (*43*−*46*) increased after protein binding (Figure 1B, spectra b−e vs spectrum a). The vinyl stretching mode $\nu_{C\alpha=C\beta}$ downshifted for H_2PP bound to the Ni^{2+}-chelatase variants, i.e., from 1627.0 cm^{-1} for the wild-type enzyme to 1623.7 cm^{-1} for S143T, 1625.8 cm^{-1} for F323L, and 1624.1 cm^{-1} for S143T/F323L) (Figure 1B).

Binding of NiPP to Directly Evolved Ni^{2+}-Chelatase Variants. To assess the effect of the single (S143T and F323L) and double mutations (S143T/F323L) on metalloporphyrin deformation, we examined the binding of NiPP to the active site of the wild-type ferrochelatase and variants. Because the porphyrin tends to contract around the small Ni(II) ion by distorting from planarity, NiPP provides an insightful probe of the porphyrin conformation in the active site. Indeed, NiPP is distorted from planarity upon binding to wild-type ferrochelatase (*26*, *34*). Figure 2 illustrates the low-frequency (Figure 2A) and high-frequency (Figure 2B) regions of the RR spectra of NiPP in equilibration buffer (Figure 2, spectrum a), NiPP incubated with wild-type ferrochelatase (Figure 2, spectrum b) and with the directly evolved variants (Figure 2, spectra c−e). When compared to unbound NiPP (Figure 2A, spectrum a), sharpening of the $\delta_{C\beta CaCb}$ bending mode and sharpening and splitting of ν_7 occurred after binding to any of the proteins (Figure 2A, spectra b−e). Although there are differences in the propionate bending modes (ν_{prop}) of protein-bound and free NiPP, there were no significant differences in the propionate modes of the variants in comparison to wild-type ferrochelatase.

In the high-frequency region of the spectra, pronounced differences in the free (Figure 2B, spectrum a) and protein-bound (Figure 2B, spectra b−e) NiPP spectra were apparent. The ν_2, ν_3, and ν_{10} structure-sensitive lines (*47*, *48*) downshifted, while the vinyl stretching mode ($\nu_{Ca=Cb}$) (*43*) increased in intensity (Figure 2B, spectra b−e vs spectrum a) as previously found for wild-type ferrochelatase (*26*) and other ferrochelatase variants (*34*). The spectral changes associated with the S143T/F323L double variant (Figure 2A and Figure 2B, spectra e), while significant, may be less than for the other variants, suggesting that this variant has a looser interaction with the porphyrin. The increased resolution of the vinyl stretching modes of NiPP (near 1630 cm^{-1}) when bound to the Ni^{2+}-chelatase variants (Figure 2B, spectra b−e) is noted for all directly evolved Ni^{2+}-chelatase variants.

Binding of Fe^{3+}-PPIX (Hemin) to Directly Evolved Ni^{2+}-Chelatase Variants. The binding interaction of hemin, a known ferrochelatase inhibitor (*49*), with the Ni^{2+}-chelatase variants was examined by comparing RR spectra of hemin bound to the variants with spectra of unbound hemin and hemin bound to wild-type ferrochelatase (Figure 3). Hemin binding to all proteins produced a shift of the ν_7 line from 674.0 cm^{-1} (Figure 3A, spectrum a) to 673.3 cm^{-1} (Figure 3A, spectra b−e). In addition, although hemin binding to any of the four proteins induced a decrease in the intensity of vinyl bending lines ($\delta_{C\beta CaCb}$), the propionate bending modes (ν_{prop}), and ν_{15} (Figure 3A, spectra b−e vs spectrum a), the variants showed no appreciable differences from the spectra of the wild-type ferrochelatase-bound hemin (Figure 3A, spectra c−e vs spectrum b).

Similar to our previous findings with wild-type ferrochelatase (*34*), the hemin structure-sensitive lines ν_2 and ν_3 (*44*, *45*) changed, in frequency and intensity, respectively, upon incubation with the Ni^{2+}-chelatase variants (Figure 3B, spectra b−e). When comparing to the unbound hemin, ν_{38}, a line associated with $C_\beta-C_\beta$ and $C_\beta-C_1$ stretches (*44*, *45*) downshifted for wild-type ferrochelatase-bound hemin, whereas it slightly upshifted in the S143T and F323L spectra. For the S143T/F323L variant, ν_{38} was weak and broad, indicating that hemin was more loosely bound to the double variant. Given that both the ν_2 and ν_{38} lines are vinyl-associated modes (*43*−*45*), the changes in these modes likely indicate conformational alterations induced by the protein near the vinyl groups of the variant-bound porphyrins. Pronounced low-frequency shoulders could be observed on the ν_4 band of the spectra of the singly mutated variants S143T and F323L (Figure 3B, spectra c and d). However, the assignment of these shoulders is uncertain as judged from the RR spectral assignments made for ferricytochrome *c* (*44*), but they probably result from a shifted E_u mode, such as ν_{41}.

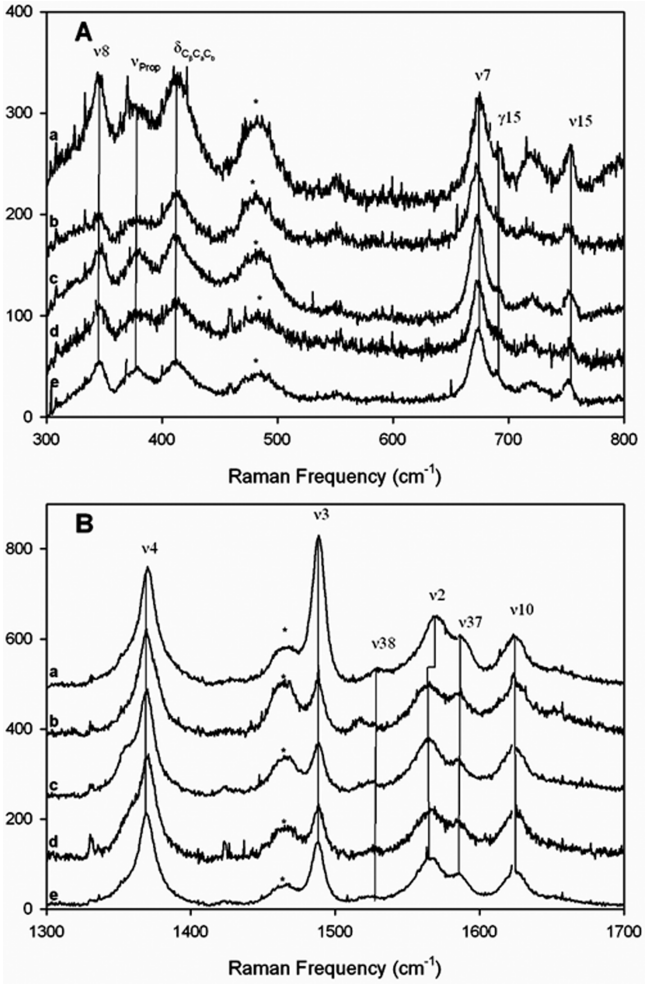

FIGURE 3: Low-frequency (A) and high-frequency (B) regions of the resonance Raman spectra of Fe^{3+}-PPIX (hemin) in assay buffer (a), bound to wild-type ferrochelatase (b), and bound to directly evolved Ni^{2+}-chelatase variants (c−g) after incubation with a protein:hemin molar ratio of 3. The variants include (c) singly mutated variant S143T, (d) singly mutated variant F323L, and (e) doubly mutated variant S143T/F323L. Asterisks denote buffer lines.

Steady-State Kinetic Analyses of Wild-Type Ferrochelatase and Directly Evolved Ni^{2+}-Chelatase Variants with either Ni^{2+} or Fe^{2+} as the Metal Ion Substrate. Since under the experimental conditions used (e.g., concentrations of Ni^{2+} lower than 40 μM and Tris buffer, pH 8.0) no Ni^{2+} substrate inhibition of ferrochelatase was observed, we fitted the steady-state kinetic data for wild-type ferrochelatase and Ni^{2+}-chelatase variants to the Michaelis−Menten equation to obtain their catalytic parameters (k_{cat}, K_m, and catalytic efficiencies (k_{cat}/K_m)). Further, even when concentrations of the metal ion substrate are inhibitory, Ni^{2+} is the least inhibitory metal ion among the metal ion substrates previously examined (Ni^{2+} Cu^{2+}, Co^{2+}, and Zn^{2+}) with an inhibitory constant of 70 μM (*23*). The determined steady-state kinetic parameters for Ni^{2+} chelation into H_2PP by wild-type ferrochelatase and the Ni^{2+}-chelatase variants are summarized in Table 1. Steady-state kinetic parameters only provide information sufficient to describe a minimal kinetic scheme (*50*); k_{cat} corresponds to the maximum rate of product formation at saturating substrate, while k_{cat}/K_m is the apparent second-order rate constant for productive substrate binding (*50*). All of the variants exhibited greater Ni^{2+}-chelatase turnovers (k_{cat}) than wild-type ferrochelatase, with the k_{cat} value for S143T being 47-fold greater than that of the wild-type enzyme, indicating that S143T produces NiPP at a considerably faster rate than wild-type ferrochelatase. Similarly, the catalytic efficiencies of the variants for H_2PP (k_{cat}/K_m^{PPIX}) were substantially increased, with the highest enhancement of over 40-fold above that of wild-type ferrochelatase for the S143T variant and the lowest enhancement (~3.7-fold) for the F323L variant. Although the catalytic efficiencies of the Ni^{2+}-chelatase variants toward Ni^{2+} ($k_{cat}/K_m^{Ni^{2+}}$) were also increased in comparison to that of wild-type ferrochelatase, the magnitude of the improvements was not as large as for H_2PP, as indicated by the lower apparent second-order rate constants for productive binding of Ni^{2+} than H_2PP (Table 1). This reflects the smaller impact that the introduced mutations (S143T, F323L, or a combination of the two) had on the Michaelis constant for H_2PP (K_m^{PPIX}) than for Ni^{2+} ($K_m^{Ni^{2+}}$).

The mutations introduced in ferrochelatase that yielded enhanced Ni^{2+}-chelatase activities surprisingly also increased the k_{cat} values of the variants toward ferrous ion incorporation into the H_2PP macrocycle (i.e., ferrochelatase activity) (Table 2). When compared to wild-type ferrochelatase, the greatest enhancements in the values of k_{cat} and catalytic efficiency for H_2PP (k_{cat}/K_m^{PPIX}) were observed for the double variant S143T/F323L (i.e., 13.4- and 4.1-fold, respectively). While the three evolved Ni^{2+}-chelatases exhibited greater catalytic efficiencies toward Fe^{2+} ($k_{cat}/K_m^{Fe^{2+}}$) than wild-type ferrochelatase, the S143T variant again exhibited the greatest enhancement (Table 2). In fact, the S143T variant was the only enzyme with a greater value for $k_{cat}/K_m^{Fe^{2+}}$ than for k_{cat}/K_m^{PPIX}, which corresponds to an ~2.8-fold higher second-order rate constant for $k_{cat}/K_m^{Fe^{2+}}$ (Table 2).

Saddling-like Porphyrin Distortion, Catalytic Efficiency, and Catalysis in Ni^{2+}- and Fe^{2+}-Chelatase-Catalyzed Reactions. Previously, we (*34*) and others (*30*) demonstrated that the degree of saddling deformation undergone by the porphyrin substrate upon binding to ferrochelatase or ferrochelatase catalytic antibodies correlates with the catalytic efficiency of the enzyme toward porphyrin. To examine if the extent of the induced porphyrin saddling affects the catalytic efficiency of the Ni^{2+}-chelatase variants toward H_2PP, we determined the relative intensity of the RR out-of-plane saddling vibrational mode γ_{15}. Previously, we used the integrated intensity of γ_{15} normalized to the intensity of ν_7 in the same spectrum as a measure of the degree of porphyrin saddling deformation induced by ferrochelatase (*34*). Of relevance, the activation of the γ_{15} mode, a B_{2u} symmetry saddling-like mode, has been attributed to a saddling deformation of the porphyrin upon binding to ferrochelatase (*26*, *34*), while the ν_7 line corresponds to an A_{1g} in-plane pyrrole ring symmetric deformation (*26*, *45*), and such an in-plane deformation is expected to accompany the saddling and other deformations that occur upon porphyrin binding (*34*). In the present study, we also referenced the integrated intensity of γ_{15} to the intensity of ν_{15}. The percentage of the intensity of γ_{15} associated with the variant-bound H_2PP relative to that of wild-type enzyme-bound H_2PP was virtually the same regardless of the normalization criterion (Table 3).

The steady-state kinetic parameters of the enzymes given in Tables 1−3 can be related to the saddling deformation as shown in Figure 4. When the catalytic efficiencies of ferrochelatase and variants toward the metal ion substrate (Ni^{2+} or Fe^{2+}) were plotted as a function of the extent of saddling undergone by the H_2PP substrate (as evaluated by either $A(\gamma_{15})/A(\nu_7)$ or $A(\gamma_{15})/A(\nu_{15})$), a relationship became apparent. The magnitude of the

Table 1: Ni^{2+}-Chelatase Activity: Summary of Steady-State Kinetic Parameters for Wild-Type Ferrochelatase and Ni^{2+}-Chelatase Variants

protein	k_{cat} (min^{-1})	K_i^{PPIX} (μM)	K_m^{PPIX} (μM)	$K_m^{Ni^{2+}}$ (μM)	k_{cat}/K_m^{PPIX} (μM^{-1} min^{-1})	$k_{cat}/K_m^{Ni^{2+}}$ (μM^{-1} min^{-1})
wild-type ferrochelatase	0.75 ± 0.04	1.54 ± 0.27	0.26 ± 0.16	22.06 ± 2.47	2.84 ± 0.23	$3.34 \times 10^{-2} \pm 4.18 \times 10^{-3}$
S143T	35.4 ± 1.6	1.70 ± 0.28	0.29 ± 0.14	65.21 ± 6.64	120.9 ± 7.8	$5.43 \times 10^{-1} \pm 6.11 \times 10^{-2}$
F323L	12.7 ± 0.5	2.22 ± 0.57	1.23 ± 0.20	32.18 ± 4.14	10.4 ± 0.5	$9.63 \times 10^{-2} \pm 5.08 \times 10^{-3}$
S143T/F323L	26.3 ± 1.2	0.90 ± 0.18	2.43 ± 0.26	103.7 ± 8.6	10.8 ± 0.8	$2.54 \times 10^{-1} \pm 2.38 \times 10^{-2}$

Table 2: Ferrochelatase Activity: Summary of Steady-State Kinetic Parameters for Wild-Type Ferrochelatase and Ni^{2+}-Chelatase Variants

protein	k_{cat} (min^{-1})	K_i^{PPIX} (μM)	K_m^{PPIX} (μM)	$K_m^{Fe^{2+}}$ (μM)	k_{cat}/K_m^{PPIX} (μM^{-1} min^{-1})	$k_{cat}/K_m^{Fe^{2+}}$ (μM^{-1} min^{-1})
wild-type ferrochelatase	8.5 ± 0.1	1.11 ± 0.26	1.72 ± 0.16	2.26 ± 0.16	4.94 ± 0.17	3.75 ± 0.23
S143T	72.7 ± 2.5	11.16 ± 1.72	8.31 ± 0.84	2.91 ± 0.27	8.74 ± 0.65	25.01 ± 1.59
F323L	96.2 ± 1.8	0.71 ± 0.17	5.47 ± 0.21	8.95 ± 0.40	17.57 ± 0.37	10.74 ± 0.31
S143T/F323L	114.2 ± 3.1	1.84 ± 0.33	5.58 ± 0.31	7.28 ± 0.47	20.43 ± 0.63	15.68 ± 0.73

Table 3: Results of Spectral Simulations for Protein-Bound Free Base Protoporphyrin IX Based on Least-Squares Fitting with Lorentzian Line Shapes for the γ_{15} Line

protein	ν_7 (cm^{-1})	intensity (area)	total intensity (area)	ν_{15} (cm^{-1})	intensity (area)	γ_{15} (cm^{-1})	intensity (area)	width	relative intensity (γ_{15}/ν_7)	% wild-type relative intensity[a]	relative intensity (γ_{15}/ν_{15})	% wild-type relative intensity[b]
wild-type ferrochelatase	673.4	1578.1	3279.8	754.8	511.8	700.2	504.8	2.67	0.1540	100.0	0.986	100.0
	677.8	1701.7										
S143T	669.6	1332.1	2287.7	751.1	370.9	695.5	96.7	2.59	0.0423	27.5	0.261	26.4
	674.6	955.6										
F323L	670.6	1026.3	2197.6	750.0	318.3	696.2	138.9	2.62	0.0632	41.1	0.436	44.2
	674.8	1171.3										
S143T/F323L	669.5	877.5	2052.3	750.3	347.7	696.6	223.8	2.46	0.1090	70.9	0.644	65.3
	637.7	1174.8										

[a]% wild-type relative intensity was determined by normalizing the relative intensity (γ_{15}/ν_7) corresponding to each variant against that of the wild-type ferrochelatase. [b]% wild-type relative intensity was determined by normalizing the relative intensity (γ_{15}/ν_{15}) corresponding to each variant against that of the wild-type ferrochelatase.

catalytic efficiency of the Ni^{2+}-chelatase variants toward Ni^{2+} ($k_{cat}/K_m^{Ni^{2+}}$) generally decreases with the degree of saddling of the porphyrin substrate although there is considerable variation among enzymes (Figure 4A). For Fe^{2+} insertion, the degree of porphyrin saddling relates to the catalytic efficiency toward Fe^{2+} ($k_{cat}/K_m^{Fe^{2+}}$) in a similar manner as that toward Ni^{2+} (Figure 4B). The turnover numbers for the enzymes showed a similar trend with the variants exhibiting higher k_{cat} values than wild-type ferrochelatase (Tables 2 and 3).

DISCUSSION

Previous resonance Raman spectroscopic studies in combination with enzyme kinetic determinations indicated a specific relationship between the primary structure of the conserved active site loop in murine ferrochelatase and porphyrin binding (*26*, *34*). Ferrochelatase variants harboring mutations in the active site loop exhibited decreased affinity for the porphyrin and induced a less pronounced distortion of the porphyrin than the wild-type enzyme (*51*). In particular, the saddling of the porphyrin induced by ferrochelatase appeared to modulate the catalytic efficiency toward the porphyrin substrate (k_{cat}/K_m^{PPIX}), and an invariant tryptophan in the active site loop (e.g., W256 in murine ferrochelatase) appeared to assume a major determinant role in inducing this nonplanar porphyrin conformation (*34*). Therefore, a saddled porphyrin conformation was suggested to be a favored distortion induced during catalysis by the active site of ferrochelatase. Support of a reduction of the ground state activation barrier for noncatalytic porphyrin metalation in polar solvents also showed preference for saddled porphyrins (*52*). Together, these studies suggested that the saddled porphyrin geometry represented the ground state distortion most favorable for porphyrin chelation of iron(II). The rationale has been that the saddled porphyrin conformation induced by wild-type ferrochelatase promotes optimal alignment of the porphyrin relative to the metal ion-binding site, thus favoring catalysis (*8*, *24*). This idea is consistent with hybrid quantum mechanical/molecular mechanics calculations, which indicate that the binding of a distorted porphyrin, particularly in a saddled conformation, is thermodynamically preferred to that of a less flexible, metalated porphyrin (*25*). This further accentuated the importance of an active site architecture for binding a distorted porphyrin and releasing a flatter, metalated porphyrin from the enzyme (*25*). However, in contrast to a 30° distortion of the porphyrin macrocycle, as observed in the porphyrin-bound *B. subtilis* ferrochelase structures (*25*, *53*), only a 10−12° distortion of the porphyrin ring was determined in the human ferrochelatase structures (*17*). In addition, recent crystal structures of human ferrochelatase with bound metalated porphyrin revealed that an active site π-helix structure undergoes substantial conformational rearrangement (*18*). While conformational heterogeneity of the π-helix has not been reported for crystal structures of *B. subtilis* ferrochelatase (*53*), an induced fit with strain mechanism has been proposed for the bacterial enzyme (*24*). Thus, although the definite sequential, structural, and kinetic details of the ferrochelatase catalyzed-porphyrin metalation steps are still

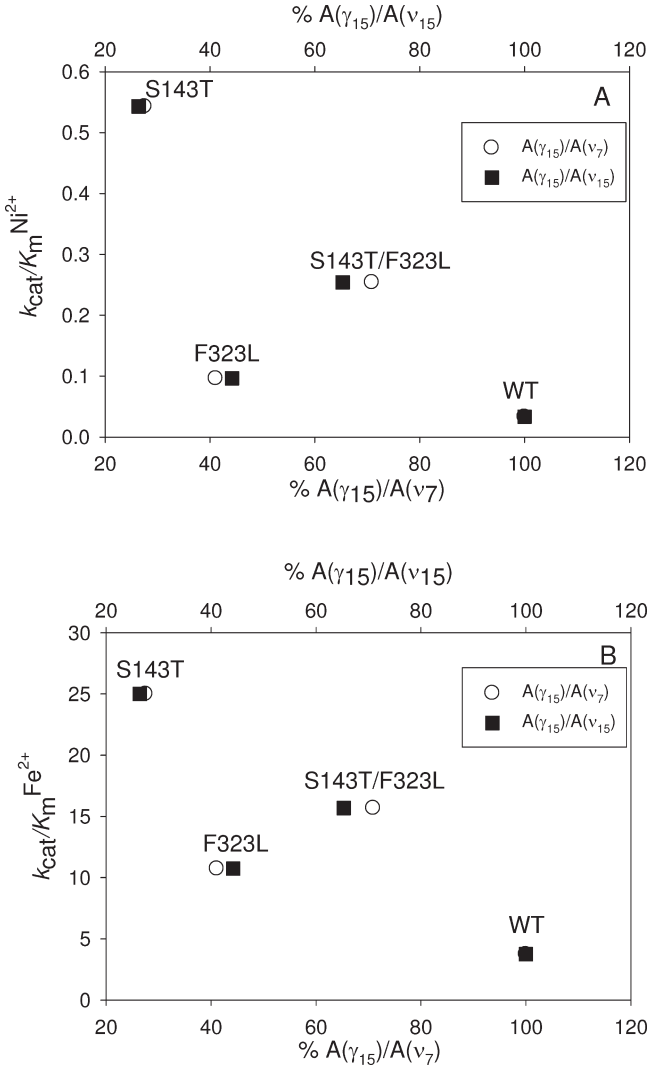

FIGURE 4: Catalytic efficiencies (k_{cat}/K_m) toward Ni^{2+} (A) and Fe^{2+} (B) insertion into H_2PP by wild-type ferrochelatase (WT) and Ni^{2+}-evolved variants (S143T, F323L, S143T/F323L) as a function of the degree of porphyrin saddling as determined by the area ratio for the γ_{15} and ν_{15} lines (or the γ_{15} and ν_7 lines).

controversial, it is generally recognized that ferrochelatase has a role in distorting of one or more porphyrin pyrrole rings out of the macrocyclic plane (*54*). In this study, using ferrochelatase variants which were selected for significantly enhanced Ni(II)-chelatase activity over that of the wild-type enzyme, we demonstrate that a reduction in the protein-induced H_2PP saddling mode is associated with a less stringent metal ion preference by ferrochelatase.

Porphyrin Distortion, Chelatase Activity, and Catalytic Efficiency. A comparative analysis of the RR spectra of H_2PP bound to the Ni^{2+}-chelatase variants (i.e., S143T, F323L, and S143T/F323L) and wild-type ferrochelatase leads us to hypothesize that the mutations introduced in the ferrochelatase scaffold to generate the Ni^{2+}-chelatase variants are the basis for distinct degrees of induced saddling of the porphyrin macrocycle, which in turn are germane to the different preferences for various divalent metal ion substrates. Porphyrin saddling occurs upon binding of H_2PP to the active site pocket of the Ni^{2+}-chelatase variants, as was previously observed for wild-type murine ferrochelatase (*26*, *33*) and murine ferrochelatase variant harboring one or more mutations in an active site loop covering residues Q248−L257 (*34*). Importantly, the catalytic efficiency (k_{cat}/K_m^{PPIX}) of ferrochelatase and the active site loop variants depended on the relative degree of saddling deformation undergone by the porphyrin substrate (*34*). In the present study, we extend this view by demonstrating that the different metal ion substrate selectivity of Ni^{2+}-chelatase variants relates to the lower degree of porphyrin saddling induced by these chelatases in relation to the parent wild-type ferrochelatase.

For Ni^{2+} chelation of protoporphyrin IX under saturating concentrations of Ni^{2+}, all three Ni^{2+}-chelatase variants exhibited greater turnover numbers (k_{cat}) and catalytic efficiencies ($k_{cat}/K_m^{Ni^{2+}}$ and k_{cat}/K_m^{PPIX}) than those of wild-type ferrochelatase (Table 1); albeit the greatest enhancements were associated with S143T, which was also the variant that distorted the porphyrin substrate the least (Table 3). The overall active site similarity among the Ni^{2+}-chelatase variants and wild-type ferrochelatase coupled to their distinct catalytic and kinetic properties reflects both the sensitivity of macrocycle conformation to small active site modifications and the relation between chelatase activity and the porphyrin macrocycle distortion. Porphyrin metalation is accepted to proceed via a "sitting-atop" (SAT) complex intermediate, in which the pyrrole nitrogen atoms are protonated and the metal ion is coordinated to both of the unprotonated pyrrole nitrogen atoms (*55*, *56*). In this presumed structure, the protons on the two pyrrole nitrogen atoms impede the metal ion from occupying the center of the porphyrin plane, and hence the metal ion remains above the macrocycle plane and also coordinated to a defined number of solvent molecules. Using theoretical methods, Shen and Ryde (*55*, *56*) obtained structural models for SAT complexes of different metalated porphyrins and determined that SAT complexes with similar energies could have different relative stabilities depending on the metal ion.

One possible interpretation for the results for the evolved Ni^{2+}-chelatase variants is that a more stable SAT complex of the metalloporphyrin is formed in the chelatase variant-catalyzed reactions; further, the stability of the SAT complex would depend on the contribution of saddling to the porphyrin distortion. The less saddled porphyrin conformers would form more stable SAT complexes than the enzyme-bound product (E−P) complex (Scheme 1). This model would explain the relaxed metal ion preference observed for the evolved Ni^{2+}-chelatase variants in relation to wild-type ferrochelatase, and it is consistent with models for nonenzymatic porphyrin metalation (*57*). The small secondary structure perturbations caused by changes to the hydrogen-bonding network would alter the Michaelis complex of H_2PP bound to the evolved Ni^{2+}-chelatase variants in comparison to that of wild-type ferrochelatase; presumably the reaction coordinate for porphyrin metalation catalyzed by the variants would display a different transition state from that for the wild-type ferrochelatase-catalyzed reaction. Therefore, when considering the minimal kinetic mechanism for chelatases, the chemical step becomes increasingly more rate-limiting (over the product release step) as the geometry of the enzyme-bound H_2PP becomes less saddled. An obvious implication of this model is that distortion and metal specificity are tunable variables directly associated with enzyme−porphyrin interaction.

The rates of metal ion incorporation into H_2PP in the yeast ferrochelatase-catalyzed reaction follow the order $Fe^{2+} > Zn^{2+} > Ni^{2+} \approx Co^{2+}$ (*23*). However, this order does not match that reported for the relative rates of the nonenzymatic metalation (i.e., $Zn^{2+} > Co^{2+} > Fe^{2+} > Ni^{2+}$) (*58*). Significantly, rates of nonenzymatic porphyrin metalation are predominantly determined

Scheme 1: Ferrochelatase-Catalyzed Reaction

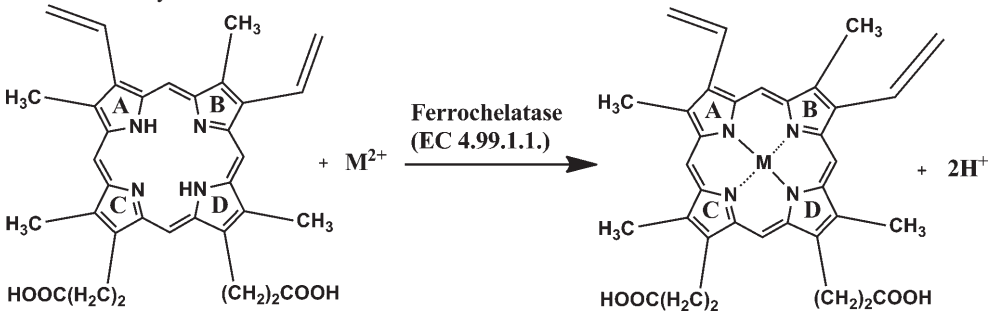

Scheme 2: Postulated Minimal Kinetic Mechanism for Ferrochelatase[a]

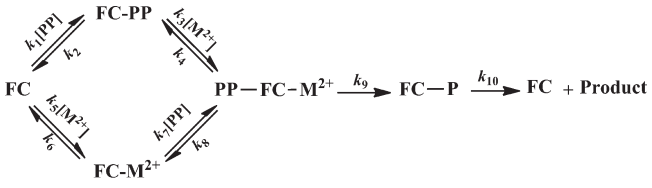

[a]FC, ferrochelatase; M^{2+}, divalent metal ion, PP, protoporphyrin IX; P, metalated protoporphyrin IX.

by rates of ligand exchange (*58*), thus implying that other "factors" should contribute to the faster release of heme over other metalloporphyrins. Indeed, the rate of product release (k_{10} in Scheme 2) appears to limit the reactions of human and murine wild-type ferrochelatases (*32*, *59*). The observation of a pre-steady-state burst of product formation during transient kinetic analyses of the human ferrochelatase-catalyzed reaction not only indicates that the rate-determining step is product release but also suggests that other metalloporphyrins are dissociated more slowly from the enzyme than heme. As a typical example of an enzyme utilizing substrate strain in biological catalysis, the decreased energy of the transition state in the ferrochelatase-catalyzed reaction is driven by the enhanced binding energy of the strained substrate to ferrochelatase (*27*, *34*). Thus, metal ion specificity in the reactions of ferrochelatase and evolved Ni^{2+}-chelatase variants are likely dependent on the thermodynamic "strain" applied toward the rate-limiting protein conformational change associated with binding a nonplanar porphyrin. While the activation barrier for the catalyzed nickel(II) chelation decreases with reduction of degree of the porphyrin saddling, the rate of iron(II) insertion into the protoporphyrin IX macrocycle increases with an increase of the extent of the saddled porphyrin deformation (Tables 1−3 and Figure 4). In sum, the contribution of the saddled porphyrin deformation to steady-state chelatase activity differs between the two metal ions.

Protein Interactions with Vinyl Groups of the Porphyrin. Similar to the wild-type and parent ferrochelatase, the Ni^{2+}-chelatase variants modulate the saddling of the porphyrin core. The interaction between porphyrin vinyl groups and the protein matrix of the wild-type enzyme is disrupted as indicated by the distinct frequency shifts and intensity changes of the vinyl-dependent resonance Raman lines. As with the binding of H_2PP to ferrochelatase (Figure 1B, spectrum b), the vinyl stretching band $\nu_{C\alpha=C\beta}$ of H_2PP was better resolved upon protein binding (Figure 1B, spectra c−e); this suggests that the protein matrix restricts the vinyl group orientation and freedom of movement. The vinyl stretch ($\nu_{C\alpha=C\beta}$) of H_2PP bound to the Ni^{2+}-chelatase variant (at 1623.7 cm^{-1} for S143T, 1625.8 cm^{-1} for F323L, and 1624.1 cm^{-1} for S143T/F323L) was downshifted when compared with that induced by wild-type ferrochelatase (1627 cm^{-1}). Since the $\nu_{C\alpha=C\beta}$ frequency is a sensitive probe of the degree of electronic conjugation (*60*, *61*), the downshift indicates that the orientation of the vinyl groups with the protein differs between Ni^{2+}-chelatase variants and wild-type ferrochelatase. Moreover, ν_2 contains C_b-C_b pyrrole stretching and is also known to be sensitive to the vinyl groups on pyrroles A and B of H_2PP. Upon binding to the wild-type protein, ν_2 displays a large upshift in frequency relative to its position in free H_2PP. Most importantly, ν_2 of the porphyrin-bound variants is downshifted and of increased relative intensity when compared to that of the wild-type enzyme.

Mechanistic Implications of Altered Metal Ion Preference. The relative rates of nonenzymatic porphyrin metalation in solution are dominated by the rates of ligand exchange (Zn^{2+} > Co^{2+} > Fe^{2+} > Ni^{2+}) (*54*, *58*, *62*). However, the insertion rates in yeast ferrochelatase-catalyzed reactions (Fe^{2+} > Zn^{2+} > Ni^{2+} ≈ Co^{2+}) (*23*) indicate that the enzyme rate is not limited solely by ligand exchange; rather, it is accelerated such that heme is produced more quickly than other metalloporphyrins. The burst of product formation in stopped-flow experiments with human ferrochelatase showed a burst of product formation, indicating that the maximal rate is controlled by the rate of product release (*54*, *63*) and suggesting that metalloporphyrins other than heme are released slowly from the enzyme. For, at least, human FC, unwinding of the π-helix is crucial for product release (*18*, *19*). Hence, protein conformational changes might have several different functions in ferrochelatase, e.g., promote porphyrin distortion, facilitate induced-fit catalysis of chelation, or assist product release (*54*). The rates assigned to Fe^{2+}-PP and Ni^{2+}-PP release (k_{cat}) in the reactions catalyzed by the three evolved Ni^{2+}-chelatase variants (S143T, F323L, and S143T/F323L) were considerably enhanced in relation to those of the wild-type ferrochelatase-catalyzed reaction (Tables 1 and 2). Yet there was a reduction in the Ni^{2+}-chelatase-induced porphyrin saddling (Table 3 and Figure 4). Our results suggest that the penalty for the rate enhancement imposed by reduced porphyrin saddling is decreased metal ion selectivity, such that metal chelation, and not product release, may become at least a partially rate-limiting step in the metal chelatase-catalyzed reactions. In fact, reaction rate-determining chelation has precedence to occur with some nonphysiological metal ions and porphyrins (e.g., Cu^{2+} and *N*-methylmesoporphyrin IX), though product release becomes infinitely slow (*64*). When compared to wild-type ferrochelatase, interaction between the Ni^{2+}-chelatase variants (in particular, S143T and F323L) and porphyrin results in reduced saddling, release of constraints on pyrrole rotation toward their adjacent vinyl groups, increased vinyl mobility and $N_{pyr}-C_a$ modulation, and, ultimately, increased use of nickel(II) ion as substrate.

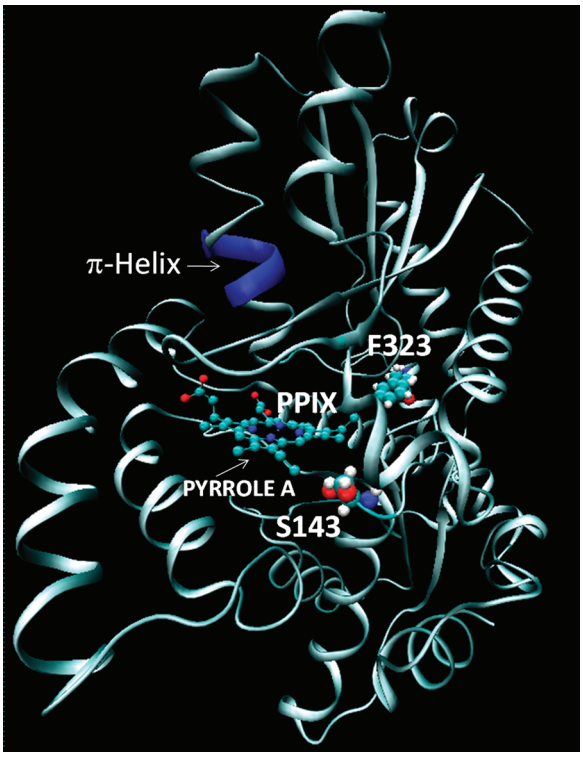

FIGURE 5: Modeled interaction between protoporphyrin IX and murine ferrochelatase. The homology structural model for murine ferrochelatase was determined using PRIME (Schrodinger, Inc.), the 1HRK human ferrochelatase tertiary structure (PDB ID: 1HRK) (*66*), and the murine ferrochelatase sequence as referred to in Shi and Ferreira (*67*). The porphyrin orientation was superimposed from the E323K human ferrochelatase variant (PDB ID: 2QD1) (*19*). Both Ser143 and Phe323 residues were labeled relative to protoporphyrin IX and pyrrole A. The π-helix is denoted in blue.

Another possible, and not necessarily mutually exclusive, interpretation relates to the identification of a second metal ion-binding site within the active site π-helix (*22*, *23*, *65*). This site is responsible for the substrate inhibition observed in *in vitro* activity assays with nonphysiological (high) substrate concentrations (*22*, *23*, *65*), and it might be a component of the metal ion substrate processing pathway (*65*). It was suggested that the second metal ion-binding site promotes reactivity, via desolvation of the Fe^{2+} atom, and modulates the release of the metal ion into the catalytic site upon winding of the π-helix (*65*). Conceivably, the introduced mutations (i.e., F323L and S143T), albeit remotely located from the active site, cause subtle structural and electrostatic changes in the porphyrin binding site, which affect the degree of porphyrin distortion and the π-helix conformational changes. The weakened saddling of the porphyrin substrate and the decreased chelation rates appear to be associated with a more promiscuous or less selective enzyme toward the metal ion substrate (Table 1−3 and Figure 5), as inferred from the smaller discrimination between the catalytic efficiencies for Fe^{2+} and Ni^{2+} of the S143T variant $[(k_{cat}/K_m^{Fe^{2+}})/(k_{cat}/K_m^{Ni^{2+}}) = 46]$ relative to that of wild-type ferrochelatase $[(k_{cat}/K_m^{Fe^{2+}})/(k_{cat}/K_m^{Ni^{2+}}) = 112]$. Finally, our proposed strategy of how the evolved variants enhance porphyrin Ni^{2+}-chelation at the expense of weakened metal ion selectivity supports the hypothesis that ferrochelatase has to remove nonplanarity from the metalated porphyrin in preparation for product release.

ACKNOWLEDGMENT

The authors thank Dr. Gregory A. Hunter (University of South Florida) and Prof. Eulália Pereira (Faculdade de Ciências, Universidade do Porto, Portugal) for helpful discussions and Mr. Chris Adams and Ms. Mallory Gillam for purifying ferrochelatase and Ni^{2+}-chelatase variants.

REFERENCES

1. Ajioka, R. S., Phillips, J. D., and Kushner, J. P. (2006) Biosynthesis of heme in mammals. *Biochim. Biophys. Acta 1763*, 723–736.
2. Hardison, R. C. (1996) A brief history of hemoglobins: plant, animal, protist, and bacteria. *Proc. Natl. Acad. Sci. U.S.A. 93*, 5675–5679.
3. Rodgers, K. R. (1999) Heme-based sensors in biological systems. *Curr. Opin. Chem. Biol. 3*, 158–167.
4. Poulos, T. L. (2005) Structural biology of heme monooxygenases. *Biochem. Biophys. Res. Commun. 338*, 337–345.
5. Padmanaban, G., Venkateswar, V., and Rangarajan, P. N. (1989) Haem as a multifunctional regulator. *Trends Biochem. Sci. 14*, 492–496.
6. Faller, M., Matsunaga, M., Yin, S., Loo, J. A., and Guo, F. (2007) Heme is involved in microRNA processing. *Nature Struct. Mol. Biol. 14*, 23–29.
7. Oates, P. S., and West, A. R. (2006) Heme in intestinal epithelial cell turnover, differentiation, detoxification, inflammation, carcinogenesis, absorption and motility. *World J. Gastroenterol. 12*, 4281–4295.
8. Dailey, H. A., and Dailey, T. A. (2003) Ferrochelatase, in The Porphyrin Handbook (Kadish, K. M., Smith, K. M., and Guilard, R., Eds.) pp 93−121, Elsevier Science, New York.
9. Ferreira, G. C. (1999) Ferrochelatase. *Int. J. Biochem. Cell Biol. 31*, 995–1000.
10. Ferreira, G. C., Franco, R., Lloyd, S. G., Moura, I., Moura, J. J. G., and Huynh, B. H. (1995) Structure and function of ferrochelatase. *J. Bioenerg. Biomembr. 27*, 221–229.
11. Bottomley, S. S. (2008) Porphyria, in Wintrobe's Clinical Hematology (Greer, P. E., et al., Eds.) 12th ed., pp 1057−1087, Lippincott & Wilkins, Baltimore, MD.
12. Kemmner, W., Wan, K., Ruttinger, S., Ebert, B., Macdonald, R., Klamm, U., and Moesta, K. T. (2008) Silencing of human ferrochelatase causes abundant protoporphyrin-IX accumulation in colon cancer. *FASEB J. 22*, 500–509.
13. Al-Karadaghi, S., Hansson, M., Nikonov, S., Jonsson, B., and Hederstedt, L. (1997) Crystal structure of ferrochelatase: the terminal enzyme in heme biosynthesis. *Structure 5*, 1501–1510.
14. Hansson, M. D., Karlberg, T., Rahardja, M. A., Al-Karadaghi, S., and Hansson, M. (2007) Amino acid residues His183 and Glu264 in *Bacillus subtilis* ferrochelatase direct and facilitate the insertion of metal ion into protoporphyrin IX. *Biochemistry 46*, 87–94.
15. Karlberg, T., Hansson, M. D., Yengo, R. K., Johansson, R., Thorvaldsen, H. O., Ferreira, G. C., Hansson, M., and Al-Karadaghi, S. (2008) Porphyrin binding and distortion and substrate specificity in the ferrochelatase reaction: the role of active site residues. *J. Mol. Biol. 378*, 1074–1083.
16. Shipovskov, S., Karlberg, T., Fodje, M., Hansson, M. D., Ferreira, G. C., Hansson, M., Reimann, C. T., and Al-Karadaghi, S. (2005) Metallation of the transition-state inhibitor N-methyl mesoporphyrin by ferrochelatase: implications for the catalytic reaction mechanism. *J. Mol. Biol. 352*, 1081–1090.
17. Medlock, A., Swartz, L., Dailey, T. A., Dailey, H. A., and Lanzilotta, W. N. (2007) Substrate interactions with human ferrochelatase. *Proc. Natl. Acad. Sci. U.S.A. 104*, 1789–1793.
18. Medlock, A. E., Carter, M., Dailey, T. A., Dailey, H. A., and Lanzilotta, W. N. (2009) Product release rather than chelation determines metal specificity for ferrochelatase. *J. Mol. Biol. 393*, 308–319.
19. Medlock, A. E., Dailey, T. A., Ross, T. A., Dailey, H. A., and Lanzilotta, W. N. (2007) A pi-helix switch selective for porphyrin deprotonation and product release in human ferrochelatase. *J. Mol. Biol. 373*, 1006–1016.
20. Wu, C. K., Dailey, H. A., Rose, J. P., Burden, A., Sellers, V. M., and Wang, B. C. (2001) The 2.0 Å structure of human ferrochelatase, the terminal enzyme of heme biosynthesis. *Nat. Struct. Biol. 8*, 156–160.
21. Karlberg, T., Lecerof, D., Gora, M., Silvegren, G., Labbe-Bois, R., Hansson, M., and Al-Karadaghi, S. (2002) Metal binding to *Saccharomyces cerevisiae* ferrochelatase. *Biochemistry 41*, 13499–13506.
22. Davidson, R. E., Chesters, C. J., and Reid, J. D. (2009) Metal ion selectivity and substrate inhibition in the metal ion chelation catalyzed by human ferrochelatase, *J. Biol. Chem.* (PMID: 19767646).

23. Hunter, G. A., Sampson, M. P., and Ferreira, G. C. (2008) Metal ion substrate inhibition of ferrochelatase. *J. Biol. Chem. 283*, 23685–23691.
24. Al-Karadaghi, S., Franco, R., Hansson, M., Shelnutt, J. A., Isaya, G., and Ferreira, G. C. (2006) Chelatases: distort to select? *Trends Biochem. Sci. 31*, 135–142.
25. Sigfridsson, E., and Ryde, U. (2003) The importance of porphyrin distortions for the ferrochelatase reaction. *J. Biol. Inorg. Chem. 8*, 273–282.
26. Lu, Y., Sousa, A., Franco, R., Mangravita, A., Ferreira, G. C., Moura, I., and Shelnutt, J. A. (2002) Binding of protoporphyrin IX and metal derivatives to the active site of wild-type mouse ferrochelatase at low porphyrin-to-protein ratios. *Biochemistry 41*, 8253–8262.
27. Romesberg, F. E., Santarsiero, B. D., Spiller, B., Yin, J., Barnes, D., Schultz, P. G., and Stevens, R. C. (1998) Structural and kinetic evidence for strain in biological catalysis. *Biochemistry 37*, 14404–14409.
28. Yin, J., Andryski, S. E., Beuscher, A. E. t., Stevens, R. C., and Schultz, P. G. (2003) Structural evidence for substrate strain in antibody catalysis. *Proc. Natl. Acad. Sci. U.S.A. 100*, 856–861.
29. Yin, J., Beuscher, A. E. t., Andryski, S. E., Stevens, R. C., and Schultz, P. G. (2003) Structural plasticity and the evolution of antibody affinity and specificity. *J. Mol. Biol. 330*, 651–656.
30. Venkateshrao, S., Yin, J., Jarzecki, A. A., Schultz, P. G., and Spiro, T. G. (2004) Porphyrin distortion during affinity maturation of a ferrochelatase antibody, monitored by resonance Raman spectroscopy. *J. Am. Chem. Soc. 126*, 16361–16367.
31. Blow, D. (2000) So do we understand how enzymes work? *Structure 8*, R77–R81.
32. Hoggins, M., Dailey, H. A., Hunter, C. N., and Reid, J. D. (2007) Direct measurement of metal ion chelation in the active site of human ferrochelatase. *Biochemistry 46*, 8121–8127.
33. Franco, R., Ma, J. G., Lu, Y., Ferreira, G. C., and Shelnutt, J. A. (2000) Porphyrin interactions with wild-type and mutant mouse ferrochelatase. *Biochemistry 39*, 2517–2529.
34. Shi, Z., Franco, R., Haddad, R., Shelnutt, J. A., and Ferreira, G. C. (2006) The conserved active-site loop residues of ferrochelatase induce porphyrin conformational changes necessary for catalysis. *Biochemistry 45*, 2904–2012.
35. Cadwell, R. C., and Joyce, G. F. (1994) Mutagenic PCR, in PCR methods and applications, Vol. 3, pp S136−S140, Cold Spring Harbor Laboratory, Cold Spring Harbor, New York.
36. Ferreira, G. C. (1994) Mammalian ferrochelatase. Overexpression in *Escherichia coli* as a soluble protein, purification and characterization. *J. Biol. Chem. 269*, 4396–4400.
37. Zhao, H., Giver, L., Shao, Z., Affholter, J. A., and Arnold, F. H. (1998) Molecular evolution by staggered extension process (StEP) *in vitro* recombination. *Nat. Biotechnol. 16*, 258–261.
38. Franco, R., Pereira, A. S., Tavares, P., Mangravita, A., Barber, M. J., Moura, I., and Ferreira, G. C. (2001) Substitution of murine ferrochelatase glutamate-287 with glutamine or alanine leads to porphyrin substrate-bound variants. *Biochem. J. 356*, 217–222.
39. Smith, P. K., Krohn, R. I., Hermanson, G. T., Mallia, A. K., Gartner, F. H., Provenzano, M. D., Fujimoto, E. K., Goeke, N. M., Olson, B. J., and Klenk, D. C. (1985) Measurement of protein using bicinchoninic acid. *Anal. Biochem. 150*, 76–85.
40. Shi, Z., and Ferreira, G. C. (2003) A continuous anaerobic fluorimetric assay for ferrochelatase by monitoring porphyrin disappearance. *Anal. Biochem. 318*, 18–24.
41. Sato, S., Aoyagi, K., Haya, T., and Kitagawa, T. (1995) Time-resolved resonance Raman study of free-base octaethylporphyrins in the S0, S1, and T1 states. *J. Phys. Chem. 99*, 7766–7775.
42. Sato, S., and Kitagawa, T. (1994) Time-resolved resonance Raman study of porphyrins and metalloporphyrins in the electronic excited states. *Appl. Phys. B: Laser Opt. 59*, 415–431.
43. Choi, S., Spiro, T. G., Langry, K. C., and Smith, K. M. (1982) Vinyl influences on protoheme resonance Raman spectra: nickel(II) protoporphyrin IX with deuterated vinyl groups. *J. Am. Chem. Soc. 104*, 4337–4344.
44. Hu, S., Morris, I. K., Singh, J. P., Smith, K. M., and Spiro, T. G. (1993) Complete assignment of cytochrome *c* resonance Raman spectra via enzymic reconstitution with isotopically labeled hemes. *J. Am. Chem. Soc. 115*, 12446–12458.
45. Hu, S., Smith, K. M., and Spiro, T. G. (1996) *J. Am. Chem. Soc. 118*, 12638–12646.
46. Sarkar, M., and Verma, A. L. (1986) Effect of vinyl groups on resonance Raman spectra of protoporphyrin-IX. *J. Raman Spectrosc. 17*, 407–414.
47. Jentzen, W., Unger, E., Karvounis, G., Shelnutt, J. A., Dreybrodt, W., and Schweitzer-Stenner, R. (1996) Conformational properties of nickel(II) octaethylporphyrin in solution. 1. Resonance excitation profiles and temperature dependence of structure-sensitive Raman lines. *J. Phys. Chem. 100*, 14184–14191.
48. Li, X. Y., Czernuszewicz, R. S., Kincaid, J. R., Stein, P., and Spiro, T. G. (1990) Consistent porphyrin force field. 2. Nickel octaethylporphyrin skeletal and substituent mode assignments from nitrogen-15, meso-d_4, and methylene-d_{16} Raman and infrared isotope shifts. *J. Phys. Chem. 94*, 47–61.
49. Dailey, H. A., and Fleming, J. E. (1983) Bovine ferrochelatase. Kinetic analysis of inhibition by N-methylprotoporphyrin, manganese, and heme. *J. Biol. Chem. 258*, 11453–11459.
50. Johnson, K. A. (1992) Transient-state kinetic analysis of enzyme reaction pathways. *Enzymes 20*, 1–61.
51. Shi, Z., Franco, R., Haddad, R., Shelnutt, J. A., and Ferreira, G. C. (2006) The conserved active-site loop residues of ferrochelatase induce porphyrin conformational changes necessary for catalysis. *Biochemistry 45*, 2904–2912.
52. Sazanovich, I. V., Galievsky, V. A., van Hoek, A., Schaafsma, T. J., Malinovskii, V. L., Holten, D., and Chirvony, V. S. (2001) Photophysical and structural properties of saddle-shaped free base porphyrins: evidence for an "orthogonal" dipole moment. *J. Phys. Chem. B 105*, 7818–7829.
53. Lecerof, D., Fodje, M., Hansson, A., Hansson, M., and Al-Karadaghi, S. (2000) Structural and mechanistic basis of porphyrin metallation by ferrochelatase. *J. Mol. Biol. 297*, 221–232.
54. Ferreira, G. C., and Hunter, G. A. (2010) Ferrochelatase structure and reaction mechanism, in The Handbook of Porphyrin Science (Kadish, K. M., Smith, K. M., and Guilard, R., Eds.) World Scientific Publishing, Hackensack, NJ.
55. Shen, Y., and Ryde, U. (2004) The structure of sitting-atop complexes of metalloporphyrins studied by theoretical methods. *J. Inorg. Biochem. 98*, 878–895.
56. Wang, Y., Shen, Y., and Ryde, U. (2009) QM/MM study of the insertion of metal ion into protoporphyrin IX by ferrochelatase. *J. Inorg. Biochem. 103*, 1680–1686.
57. Shen, Y., and Ryde, U. (2004) The structure of sitting-atop complexes of metalloporphyrins studied by theoretical methods. *J. Inorg. Biochem. 98*, 878–895.
58. Hambright, P., and Chock, P. B. (1974) Metal-porphyrin interactions. III. A dissociative-interchange mechanism for metal ion incorporation into porphyrin molecules. *J. Am. Chem. Soc. 96*, 3123–3131.
59. Shi, Z., and Ferreira, G. C. (2006) Modulation of inhibition of ferrochelatase by *N*-methylprotoporphyrin. *Biochem. J. 399*, 21–28.
60. Kalsbeck, W. A., Ghosh, A., Pandey, K. P., Smith, K. M., and Bocian, D. F. (1995) Determinants of the vinyl stretching frequency in protoporphyrins. Implications for cofactor-protein interactions in heme proteins. *J. Am. Chem. Soc. 117*, 10959–10968.
61. Marzocchi, M. P., and Smulevich, G. (2003) Relationship between heme vinyl conformation and the protein matrix in peroxidases. *J. Raman Spectrosc. 34*, 725–736.
62. Fleischer, E. B., Choi, E. I., Hambright, P., and Stone, A. (1964) Porphyrin studies: kinetics of metalloporphyrin formation. *Inorg. Chem. 3*, 1284–1287.
63. Hoggins, M., Dailey, H. A., Hunter, C. N., and Reid, J. D. (2007) Direct measurement of metal ion chelation in the active site of human ferrochelatase. *Biochemistry 46*, 8121–8127.
64. Shipovskov, S., Karlberg, T., Fodje, M., Hansson, M. D., Ferreira, G. C., Hansson, M., Reimann, C. T., and Al-Karadaghi, S. (2005) Metallation of the transition-state inhibitor N-methyl mesoporphyrin by ferrochelatase: implications for the catalytic reaction mechanism. *J. Mol. Biol. 352*, 1081–1090.
65. Hunter, G. A., and Ferreira, G. C. (2010) Identification and characterization of an inhibitory metal ion-binding site in ferrochelatase *J. Biol. Chem.* (PMID: 20966079) (doi: 10.1074/jbc.M1110.174243).
66. Wu, C. K., Dailey, H. A., Rose, J. P., Burden, A., Sellers, V. M., and Wang, B. C. (2001) The 2.0 Å structure of human ferrochelatase, the terminal enzyme of heme biosynthesis. *Nat. Struct. Biol. 8*, 156–160.
67. Shi, Z., and Ferreira, G. C. (2004) Probing the active site loop motif of murine ferrochelatase by random mutagenesis. *J. Biol. Chem. 279*, 19977–19986.